IEEE Access
Multidisciplinary | Rapid Review | Open Access Journal

Received October 10, 2019, accepted October 28, 2019, date of publication November 8, 2019, date of current version November 21, 2019.

Digital Object Identifier 10.1109/ACCESS.2019.2952371

Implementation Issues of Flux Linkage Estimation on Permanent Magnet Machine Position Sensorless Drive at Low Speed

GUAN-REN CHEN, (Student Member, IEEE), JYUN-YOU CHEN, (Student Member, IEEE), AND SHIH-CHIN YANG, (Senior Member, IEEE)

Department of Mechanical Engineering, National Taiwan University, Taipei 10617, Taiwan

Corresponding author: Shih-Chin Yang (scy99@ntu.edu.tw)

This work was supported by the Taiwanese Ministry of Science and Technology under the Grant 106-2628-E-002-014-MY3.

ABSTRACT This paper improves the surface permanent magnet (PM) machine position sensorless drive at low speed. Considering the surface PM machine (SPM) drive, EMF voltage or flux linkage should be estimated for the sensorless drive. Different from EMF voltage, the flux linkage based on the voltage integration is theoretically independent to speed which is suited for the low speed position estimation. In this paper, several improvements on the flux-based sensorless drive are proposed to enhance the low speed dynamic performance. First, a modified voltage integration is develop to remove the flux estimation drift caused by voltage or current offset. This integration contains a high-pass filter (HPF) for the DC drift elimination. In addtion, the filter delay is compensated to maintain the flux phase. Second, inverter deadtime harmonics are decoupled with the knowledge of actual machine phase voltages. It is shown that the position estimation error is decreased for the better low speed performance. According to experimental results, SPM machine sensorless drive is enhanced at 4%∼ 6% speed region from many aspects. They include position signal SNR, position error and drive dynamic response. More importantly, the overall current regulation bandwidth can increase to 1kHz at low speed. It is compatible to standard encoder-based field oriented control (FOC) drives.

INDEX TERMS Permanent magnet machine, flux observer and position sensorless drive.

I. INTRODUCTION

For SPM machine sensorless drives, the rotor position relies on spatial signal in back EMF voltage. Since EMF voltage is a speed dependent voltage function, the SNR of EMF estimation decreases as rotor speed decreases. It lead to the sensorless drive limitation at very low and zero speed because of insufficient EMF voltage magnitude [1]. As reported in [2], considerable speed estimation noises appear when the drive is operated below 10% rated speed, leading to stability issues.

Inverter deadtime harmonics are the primary issue to degrade the EMF-based sensorless drive at low speed. To reduce deadtime harmonics in EMF-based drives, a feed-forward voltage error compensation is developed based on the machine and inverter model [3], [4]. However, this feed-forward compensation requires instantaneous position signal to develop an accurate inverter deadtime model. For EMF-based drive at low speed, considerable errors are resultant due to low EMF estimation SNR [3]. On the other hand, the position estimation with a low bandwidth phase locked loop (PLL) is commonly applied to remove deadtime harmonics [5]. Although EMF-based drive can be stabilized at low speed without inverter harmonics, the dynamic response must degrade due to the low estimation bandwidth even if both observer and PLL are well designed [6]. For SPM machine sensorless drive at low speed, it is still a challenge to maintain both drive stability and controller bandwidth. This limitation blocks SPM machine sensorless drives from the progress into high-performance motion applications.

Instead of back EMF, the magnet flux linkage estimation is proposed to improve the sensorless drive performance. In general, flux linkage can be estimated through two analytical machine models, e.g. current model [7]–[10] and voltage model [9], [11]–[16]. Considering the estimation using

The associate editor coordinating the review of this manuscript and approving it for publication was Natarajan Prabaharan.

current model, flux is directly calculated by the multiplication of current and machine inductance. Because the inductance might vary at different load conditions, current-based flux estimation results in the considerable inductance parameter sensitivity [17]. By contrast, the voltage model obtains flux directly by integrating the EMF voltage. For normal speed operation, reduced parameter sensitivity is achieved. It should be noted that the voltage-based flux estimation leads to two implementation issues when EMF magnitude is insufficient at low speed. They are flux offset caused by the pure integration [11], [18], [19] and inverter deadtime harmonics [12]. A bandwidth-varying integration scheme is proposed in [11], [18]. However, both methods cannot provide the sufficient attenuation on flux offset especially at low speed. In order to resolve the flux integration issue, the current model can be integrated into the voltage model to achieve a full-region flux estimation [7], [8]. However for the flux estimation at low speed, the current based model is still dominant. Under this effect, the inductance parameter variation causes the stability issue on flux-based sensorless drives.

This paper improves the flux linkage estimation for SPM machine position sensorless drive at low speed. To avoid the influence of inductance saturation on the flux estimation, the proposed flux observer is based on the voltage model from [9], [11]–[16] to reduce the parameter sensitivity. Several enhancements are added to maintain the estimation accuracy at low speed. First, a modified integration is developed to remove the flux drift caused by voltage or current offset. This integration contains a HPF for the flux drift elimination. In addition, the filter delay is compensated from another HPF to maintain the accurate flux phase. Comparing to prior integration methods [11], [18], [19], the flux estimation bandwidth can be maintained because of this additional phase delay compensator. Second, inverter deadtime harmonics are decoupled with the knowledge of actual machine phase voltages. For the proposed flux estimation, machine voltages are obtained through the real-time digital integration of pulse width modulation (PWM) voltages. It is observed that the deadtime harmonics are removed on the flux-based position estimation. By applying these two improvements, the sensorless drive achieves the better performance among the estimation signal SNR, position errors and dynamic response. More importantly, the overall current regulation bandwidth is enhanced to 1kHz at low speed. It is compatible to standard encoder-based drives.

II. CONVENTIONAL EMF AND FLUX ESTIMATION

For SPM machine sensorless drives, the rotor position can be obtained from either the spatial signal in EMF voltage or magnet flux. This section compares the estimation signal process and required machine parameters respectively for EMF and flux estimation. Key limitations on the EMF estimation are explained.

A. EMF ESTIMATION OF PM MACHINES

The analytical model of SPM machine is shown by (1) in $\alpha\beta$ stator-referred stationary frame, where the subscript $\alpha\beta$ represents the complex vector, $F_{\alpha\beta} = f_\alpha + jf_\beta$.

$$V_{\alpha\beta} = R_s I_{\alpha\beta} + L_s \frac{d}{dt} I_{\alpha\beta} + E_{\alpha\beta} = R_s I_{\alpha\beta} + L_s \frac{d}{dt} I_{\alpha\beta} + \omega_e |\lambda_{pm}| \tag{1}$$

In (1), $V_{\alpha\beta}$ and $I_{\alpha\beta}$ are stator $\alpha\beta$ voltages and currents, R_s and L_s are the phase resistance and inductance, $E_{\alpha\beta}$ are $\alpha\beta$ EMF voltages, $|\lambda_{pm}|$ is the magnet flux magnitude, and ω_e is the rotor speed. With the parameter knowledge of R_s and L_s, the EMF voltage $E_{\alpha\beta}$ can be estimated by (2).

$$\begin{aligned} \hat{E}_{\alpha\beta} &= \begin{bmatrix} \hat{e}_a \\ \hat{e}_\beta \end{bmatrix} \begin{bmatrix} v_\alpha - \hat{R}_s & i_\alpha - \hat{L}_s di_\alpha/dt \\ \hat{v}_\beta - \hat{R}_s & i_\beta - \hat{L}_s di_\beta/dt \end{bmatrix} \\ &= \hat{\omega}_e \left|\hat{\lambda}_{pm}\right| \begin{bmatrix} -\sin\hat{\theta}_e \\ \cos\hat{\theta}_e \end{bmatrix} \end{aligned} \tag{2}$$

In (2), the superscript ^ represents the estimated variable, and $|\hat{\lambda}_{pm}|$, $\hat{\omega}_e$ and $\hat{\theta}_e$ are respectively the estimated magnet flux magnitude, estimated speed and estimated position. Besides, $\hat{R}_s$ and $\hat{L}_s$ are estimated resistance and inductance which might vary dependent on windings temperature and flux saturation. For the EMF-based sensorless drive, the position signal $\hat{\theta}_e$ in $\hat{E}_{\alpha\beta}$ can be used for FOC. However, it is observed that the magnitude of $\hat{E}_{\alpha\beta}$ is proportional to the rotor speed. At very low speed when $\omega_e \approx 0$, considerable estimation errors on $\hat{\theta}_e$ must appear because $\hat{E}_{\alpha\beta}$ is insufficient low.

B. FLUX ESTIMATION OF PM MACHINE

On the other hand, the machine magnet flux linkage also contains the spatial signal useful for the position estimation. In general, the magnet flux $\lambda_{\alpha\beta\_pm}$ in stator $\alpha\beta$ frame is equal to the integration of EMF voltage, as given by

$$\hat{\lambda}_{a\beta\_pm} = \begin{bmatrix} \hat{\lambda}_{\alpha\_pm} \\ \hat{\lambda}_{\beta\_pm} \end{bmatrix} = \int_0^t E_{a\beta} dt = |\lambda_{pm}| \begin{bmatrix} \cos\theta_e \\ \sin\theta_e \end{bmatrix} \tag{3}$$

As seen in (3), $\lambda_{\alpha\beta\_pm}$ is theoretically independent to the rotor speed, leading to the better estimation performance at very low speed. However, it is not an easy task to measure the magnet flux in standard machine drives based on the direct flux measurement. At this time, the flux estimation relies on analytical models using drive available current and voltage signals.

In general, the overall stator $\alpha\beta$ flux linkage $\lambda_{\alpha\beta}$ can be estimated using either the current model [7], [8] or voltage model [11]. Their corresponding flux estimation processes are illustrated in Fig. 1.

On the basis, the current-based flux linkage estimation is illustrated by

$$\begin{bmatrix} \hat{\lambda}_a \\ \hat{\lambda}_\beta \end{bmatrix} = \begin{bmatrix} \hat{L}_s & 0 \\ 0 & \hat{L}_s \end{bmatrix} \begin{bmatrix} i_\alpha \\ i_\beta \end{bmatrix} + \begin{bmatrix} \hat{\lambda}_{\alpha\_pm} \\ \hat{\lambda}_{\beta\_pm} \end{bmatrix} \tag{4}$$

As seen from (4), it is not possible to obtain $\lambda_{\alpha\beta\_pm}$ using drive feedback currents, $I_{\alpha\beta}$. Under this effect, the current-based model is not suited for the flux-based position estimation. On the other hand, the flux linkage $\lambda_{\alpha\beta}$ can be estimated

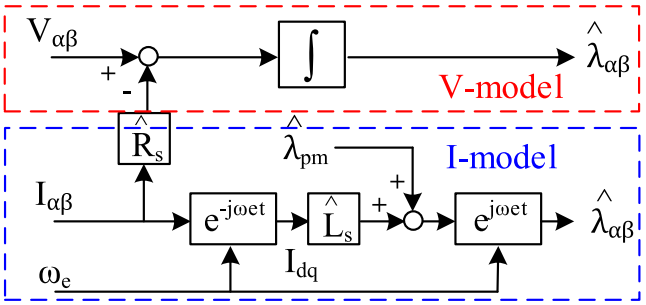

FIGURE 1. Illustration of voltage-based and current-based flux linkage estimation.

through the voltage model, which is depicted in (5).

$$\begin{bmatrix}\hat{\lambda}_\alpha \\ \hat{\lambda}_\beta\end{bmatrix} = \int_0^t \begin{bmatrix} v_\alpha - i_\alpha \hat{R}_s \\ v_\beta - i_\beta \hat{R}_s \end{bmatrix} dt \quad \text{and}$$
$$\begin{bmatrix}\hat{\lambda}_{\alpha\_pm} \\ \hat{\lambda}_{\beta\_pm}\end{bmatrix} = \begin{bmatrix}\hat{\lambda}_a \\ \hat{\lambda}_\beta\end{bmatrix} - \begin{bmatrix}\hat{L}_s & 0 \\ 0 & \hat{L}_s\end{bmatrix}\begin{bmatrix} i_\alpha \\ i_\beta\end{bmatrix} = \left|\hat{\lambda}_{pm}\right| \begin{bmatrix}\cos\hat{\theta}_e \\ \sin\hat{\theta}_e\end{bmatrix} \tag{5}$$

where $\lambda_{\alpha\beta}$ is obtained based on the integration of flux reflected voltage component. After that, the magnet flux $\lambda_{\alpha\beta\_pm}$ is estimated by subtracting the inductive induced flux $\hat{L}_s I_{\alpha\beta}$ from $\lambda_{\alpha\beta}$. Similar to EMF estimation $\hat{E}_{\alpha\beta}$ in (2), $\hat{\theta}_e$ can be extracted from magnet flux $\hat{\lambda}_{pm\_\alpha\beta}$. More importantly, the magnitudes of $\hat{\lambda}_{pm\_\alpha\beta}$ are independent to the rotor speed. Thus, a better SNR of flux-based position estimation is concluded at low speed.

C. FLUX ESTIMATION OFFSET

It is noteworthy that a voltage integration process is required to estimate the flux linkage $\hat{\lambda}_{\alpha\beta}$ in (5). Considering the real-time implementation, the voltage integration at different initial angles causes DC offsets in estimated fluxes. Fig. 2 illustrates the simulation of $\hat{\lambda}_{\alpha\beta}$ estimation through $V_{\alpha\beta}$ integration. In this simulation, the voltage initial angle is set at 45deg. It is shown that DC offsets are resultant in both $\hat{\lambda}_\alpha$ and $\hat{\lambda}_\beta$. This integration offset can be analyzed by

$$\begin{aligned}\begin{bmatrix}\hat{\lambda}_a \\ \hat{\lambda}_\beta\end{bmatrix} &= \hat{\omega}_e \left|\hat{\lambda}_{pm}\right| \int_0^t \begin{bmatrix} -\sin(\theta_e + \theta_0) \\ \cos(\theta_e + \theta_0)\end{bmatrix} dt \\ &= \left|\hat{\lambda}_{pm}\right| \begin{bmatrix}\cos(\theta_e + \theta_o) \\ \sin(\theta_e + \theta_o)\end{bmatrix} + \frac{1}{\hat{\omega}_e}\begin{bmatrix} -\cos\theta_0 \\ -\sin\theta_0\end{bmatrix}\end{aligned} \tag{6}$$

where θ_o is the corresponding voltage initial angle. This flux offset results in a 1st-order harmonic on the position estimation. Nevertheless, this offset can be compensated based on the analytical model in (6) if θ_o is known during the initial integration.

D. FLUX ESTIMATION DRIFT

A small amount of DC offset might also occur on current measurement in standard drives. Because current offset is continuously accumulated during integration, the drift on the flux estimation might result, leading to the divergence of integration process [12]. Fig. 3 shows the simulation of

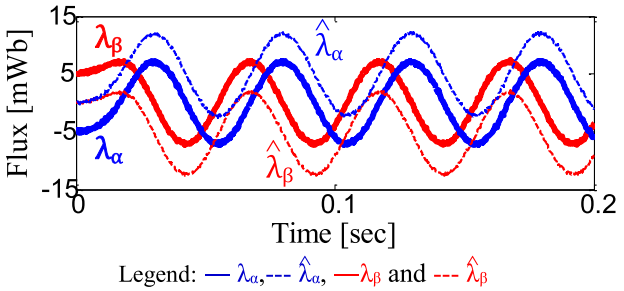

FIGURE 2. Illustration of flux estimation offset caused by the integration under different voltage initial angles.

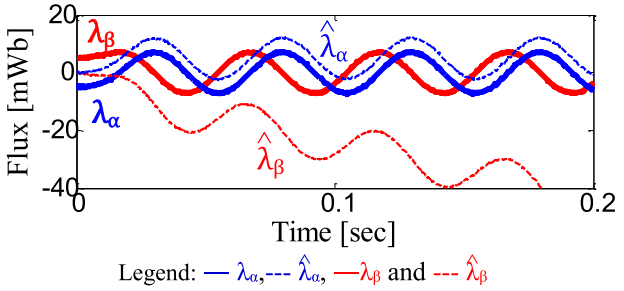

FIGURE 3. Flux estimation drift caused by the current measurement offset (5% offset in i_b).

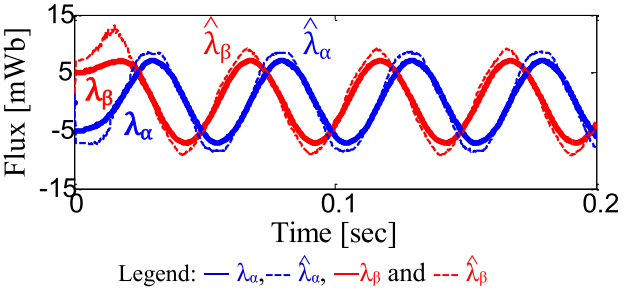

FIGURE 4. Flux estimation harmonics and magnitude error reflected by the inverter deadtime voltage distortion (2μs deadtime over 100 μs PWM).

$\hat{\lambda}_{\alpha\beta}$ estimation when a 5% offset occurs on B-phase current. As mentioned in (5), the integration drift quickly occurs on $\hat{\lambda}_\beta$. This drift must be compensated in real-time to stabilize the flux-based sensorless drive.

E. INVERTER DEADTIME HARMONICS

Inverter deadtime nonlinear effect causes additional integration errors on the flux estimation. Considering the inverter deadtime, 6th-order harmonics and magnitude drop appear on machine phase voltages. Equivalent deadtime harmonics also occur on the flux estimation because the flux is based on the voltage integration. Fig. 4 illustrates time-domain waveforms of $\hat{\lambda}_{\alpha\beta}$ estimation when 2μs deadtime is simulated in phase voltages under 10kHz PWM frequency. It is shown that the magnitude errors still appear on $\hat{\lambda}_{\alpha\beta}$. However, 6th-order harmonics are reduced because the integration is equivalent to a low-pass filter which can remove high frequency harmonics. Nevertheless, the DC flux offset leads to the position estimation error, especially at very low speed. In next section, these flux estimation issues will be resolved based on the proposed flux-based position estimation.

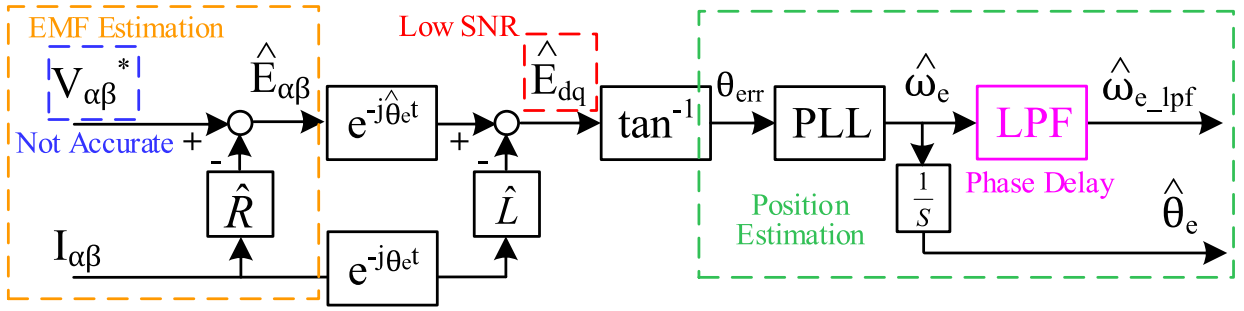

FIGURE 5. Position and speed estimation based on the spatial information in EMF voltage estimation.

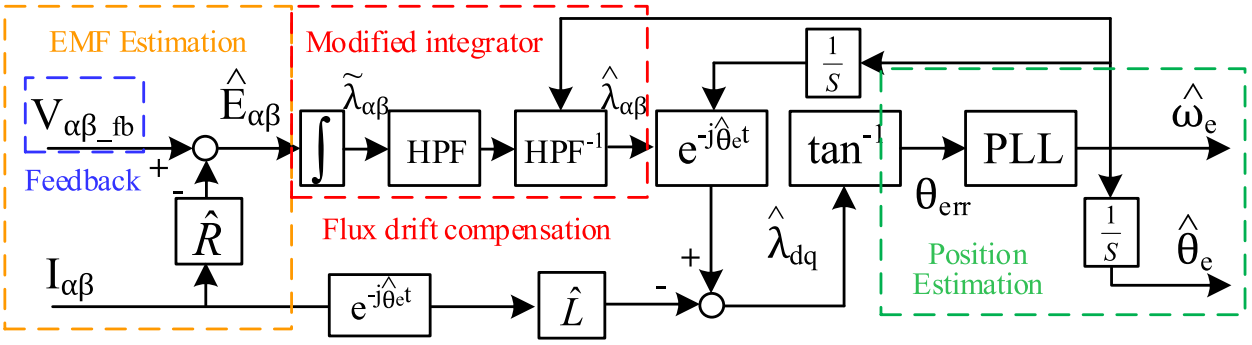

FIGURE 6. Position and speed estimation based on the spatial information in proposed magnet flux estimation.

III. PROPOSED FLUX AND POSITION ESTIMATION

This section explains the limitation on the position estimation using EMF voltage. The flux-based position estimation is then proposed to improve the low speed sensorless drive performance.

Fig. 5 illustrates the overall signal flowchart of conventional EMF-based position and speed estimation. First, $\alpha\beta$ EMF voltages $\hat{E}_{\alpha\beta}$ are estimated through the machine model in (2). After that, dq EMF voltages $\hat{E}_{\alpha\beta}$ are obtained based on the frame transformation. Assuming the rotor position is unknown at initial state, a position error θ_{err} appears between estimated dq' frame and actual dq frame [6]. The corresponding $\hat{E}_{dq'}$ in estimated dq frame is given by

$$\hat{E}_{dq'} = \hat{\omega}\left|\hat{\lambda}_{pm}\right|\begin{bmatrix} -\sin\hat{\theta}_{err} \\ \cos\hat{\theta}_{err} \end{bmatrix} \tag{7}$$

As seen in (7), the rotor position can be estimated by regulating θ_{err} in $\hat{E}_{dq'}$ to be zero. On the basis, an arctangent function is applied to obtain θ_{err} with per unit length. A phase-locked loop (PLL) is then developed for the position $\hat{\theta}_e$ and speed $\hat{\omega}_e$ estimation. Considering the low SNR of $\hat{E}_{dq'}$ at low speed, a low bandwidth PLL should be designed to remove EMF estimation noises. In addition for the speed closed-loop control, an additional LPF denoted by the purple frame in Fig. 5 is used to obtain a smooth $\hat{\omega}_e$. By adding a low PLL bandwidth and a LPF, the drive dynamic response significantly decreases at low speed. More importantly, deadtime harmonics appear on $\hat{\theta}_e$ because of low $\hat{E}_{dq'}$ SNR. It is seen that the speed dependent EMF voltage and inverter deadtime are primary issues to limit conventional EMF-based sensorless drives.

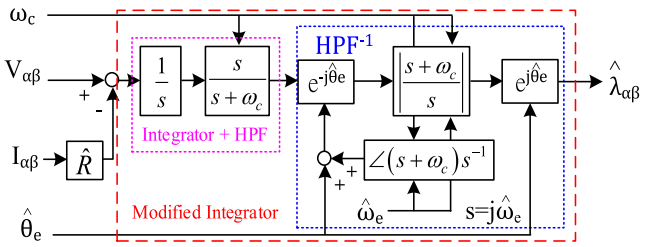

FIGURE 7. Proposed equivalent integration process based on a LPF and an inverse function of HPF.

To overcome these low speed limitations, a speed independent flux-based position estimation is proposed. Fig. 6 demonstrates the position and speed estimation based on the proposed flux observer. Comparing to existing flux estimation, three modifications are developed to improve the flux estimation at low speed.

A. MODIFIED INTEGRATION PROCESS

First, a modified integration is developed in Fig. 7. This integration process is illustrated by the red frame inside the overall flux estimation process in Fig. 6. As mentioned in section II part C and D, the pure integration of EMF voltage leads to the flux offset and drift, causing the drive stability issue. The frequency response of voltage integration process is illustrated in Fig. 8. The pure integration is equivalent to a −20dB/decade attenuation where the magnitude is respectively infinity at 0Hz and zero at ∞Hz. Once a small offset occurs on machine voltages, the resulting flux magnitude theoretically becomes infinity, leading to the flux drift.

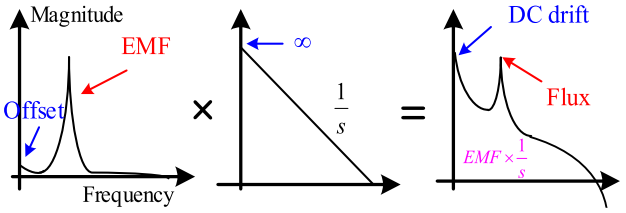

FIGURE 8. Illustration of flux estimation drift due to the integration of voltage offset.

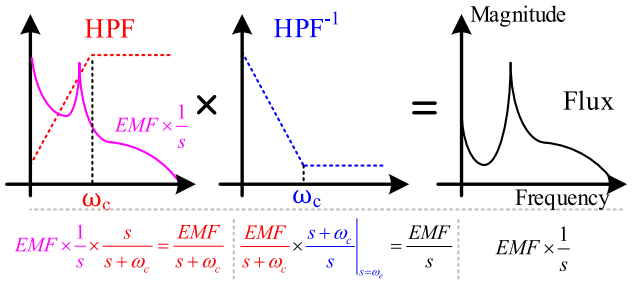

FIGURE 9. Flux estimation using the proposed integration with the filter delay compensation.

In this paper, the voltage integration is modified by Fig. 7 through i) an integrator plus a HPF denoted by the pink frame, and ii) an inverse function of HPF with the blue frame. An equivalent integration process is resultant by combining these two filters together. The proposed integration is based on [11]. However, the filter delay compensation is added for better dynamic response. Fig. 9 shows the proposed voltage integration. The equivalent transfer function is given by

$$x(t)\frac{1}{s} = \left[x(t)\frac{s}{s+\omega_c} \times \frac{1}{s}\right] \times \left.\frac{s+\omega_c}{s}\right|_{s=\omega_e} \tag{8}$$

where x(t) represents the integration variable, ω_c is the cutoff frequency of these two filters, and ω_e is the rotor speed. During the first integration, the DC offset is removed by the HPF. As seen in Fig. 9, the combination of pure integration and HPF is equivalent to a LPF. However different from the pure integration, HPF results in the phase lag and magnitude attenuation when the rotor frequency is below ω_c. Under this effect, the magnitude and phase are corrected through the second filter process in Fig. 7. On the basis, the compensation is implemented based on the inverse function of HPF with the knowledge of ω_c and ω_e.

The selection of ω_c is explained as follows. Since the first HPF is responsible for DC drift elimination, ω_c is selected not too close to DC in order to ensure the attenuation ratio. The location of ω_c is suggested at 100Hz with two-decade away from 1Hz to achieve −40dB attenuation ratio. By contrast, the filter delay is also compensated through the inverse function of HPF, as seen in Fig. 7 blue frame. Both the magnitude error and phase lag are corrected based on the frame transformation in the rotor frame. Finally, the integrated stator flux $\hat{\lambda}_{\alpha\beta}$ is obtained after the proposed integration. For the sensorless drive, the position $\hat{\theta}_e$ and speed $\hat{\omega}_e$ are calculated using the same PLL in Fig. 5.

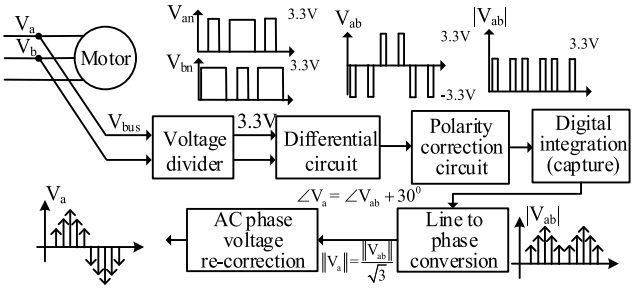

FIGURE 10. Illustration of proposed phase voltage measurement process.

B. DIRECT PHASE VOLTAGE MEASUREMENT

As mentioned in section II part E, inverter deadtime harmonics cause voltage harmonics during the flux estimation. At this part, the actual machine phase voltages are measured to remove deadtime harmonics for the voltage integration. In [20], machine phase voltages are obtained based on the digital integration through drive controller available capture module. This paper extends this voltage measurement on the flux linkage estimation.

Fig. 10 shows the signal flowchart for the phase voltage measurement. First, line-to-line PWM voltages are measured using differential circuits. After that, the digital integration is performed to obtain acutal line voltages thorugh the controller capture modulator. Finally, machine phase voltages are reconstructed based on the relationship between line voltage and phase voltage.

It is noted that the voltage measurement resolution is dependent on the capture frequency. Considering the proposed capture modulator with 150MHz frequency, a 12-bit resolution is ahcieved with the capability of 0.1% measruable PWM duty cycle. This resolution is sufficient to obtain voltages on standard industrial drives since the deadtime duty cycle is typically selected below 2%. It is important that the voltage distortion due to inverter harmonics are considered by obtaining acutal machine phase voltages. Under this effect, deadtime harmonics are insensitive to the flux linkage estimation. For the proposed drive in Fig. 6, measured voltages instead of command voltages are used for the integration. The better dynamic response can be achieved by decoupling inverter deadtime harmonics.

C. SPEED ESTIMATION WITHOUT LPF

As seen from the flux estimation process in Fig. 6, the LPF illustrated by pink frame in Fig. 5 is removed for $\hat{\omega}_e$ estimation. It is noted that the proposed voltage integration is equivalent to an infinite impulse response filter with the capability to reject high frequency noises. Without additional LPF, the dynamic response of $\hat{\omega}_e$ can be maintained. Under this effect, the SNR of $\hat{\omega}_e$ should improve. It leads to a better dynamic response using the flux-based sensorless drive at low speed.

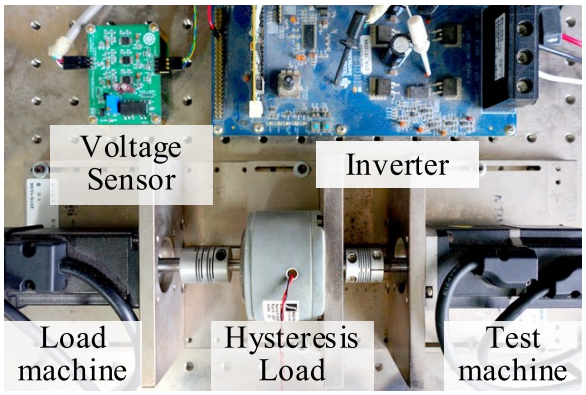

FIGURE 11. Bench of PM machine flux-based sensorless drive.

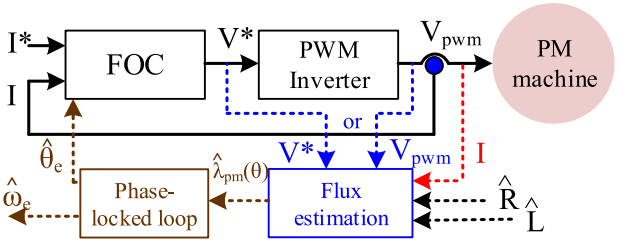

FIGURE 12. Position sensorless drive based on EMF or flux-based position estimation.

IV. EXPERIMENTAL RESULTS

An 8-pole surface PM machine with the rated speed of 3000rpm is used to evaluate the flux-based position sensorless drive. Fig. 11 shows the photograph of the test bench. A hysteresis dyno is coupled with the test machine to apply torque load. An incremental encoder is attached on the test machine to measure the actual rotor speed for comparison only. All sensorless drive algorithms are implemented in a 32-bit microcontroller, TI-TMS320F28069. Key test machine characteristics are listed in Table 1. The overall signal flowchart of flux-based sensorless drive is illustrated in Fig. 12. In this paper, a comparative evaluation between flux-based and EMF-based sensorless drive is performed among the signal SNR, position error, harmonic distortion, closed-loop drive bandwidth, and dynamic response.

A. ESTIMATED EMF vs. ESTIMATED FLUX WAVEFORMS

This part evaluates both the EMF and flux estimation waveforms at different loads. Fig. 13 shows XY patterns of $\hat{e}_\alpha$ versus $\hat{e}_\beta$, and $\hat{\lambda}_{pm\_\alpha}$ versus $\hat{\lambda}_{pm\_\beta}$ at different load conditions. In this experiment, $\hat{e}_\alpha$ and $\hat{e}_\beta$ are estimated based on (2) while $\hat{\lambda}_{pm\_\alpha}$ and $\hat{\lambda}_{pm\_\beta}$ are obtained from (5). The phase voltage measurement in Fig. 10 is added for both EMF and flux estimation. The current controller bandwidth is set at 1000Hz and the rotor speed is controlled to maintain 2% rated speed (60rpm). As seen from Fig. 13(a), considerable noises appear on the EMF pattern $\hat{e}_\alpha$ versus $\hat{e}_\beta$ where the radius varies between 0.51∼ 0.72V. More importantly at full load in (b), the pattern of $\hat{e}_\alpha$ versus $\hat{e}_\beta$ significantly distorts from a circle where the radius changes between 0.45∼ 1.17V. Because the magnitudes of $\hat{e}_\alpha$ and $\hat{e}_\beta$ are dependent on the speed, the SNR decreases at low speed even with the phase voltage measurement. Under this effect, the dynamic response must degrade for the EMF-based drive at low speed.

TABLE 1. Test PM machine characteristics.

Characteristics	Values
Rotor poles	8-pole
Rated torque	0.16Nm
Rated current	1A
Rated speed	3000rpm (200Hz elec frequency)
Resistance	4.7Ω
Inductance	4.7mH
EMF constatnt	0.0107 V/rpm
PWM frequency	10kHz
DC bus voltage	50V

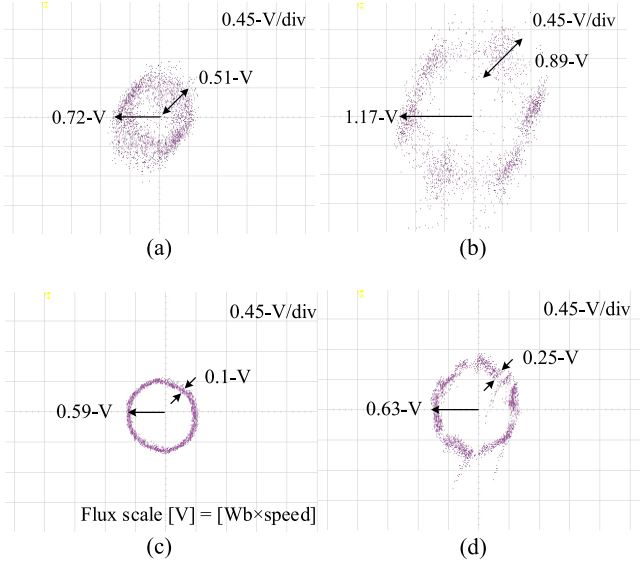

FIGURE 13. EMF and flux estimation by evaluating the pattern of $\hat{e}_\alpha$ versus $\hat{e}_\beta$ at (a) no load and (b) full load, and $\hat{\lambda}_{pm\_\alpha}$ versus $\hat{\lambda}_{pm\_\beta}$ at (c) no load and (d) full load (60 rpm speed, 1000Hz current bandwidth and phase voltage measurement).

By contrast, Fig. 13(c) illustrates the XY pattern of $\hat{\lambda}_{pm\_\alpha}$ versus $\hat{\lambda}_{pm\_\beta}$ at no load. To easily compare the flux waveform with prior EMF waveforms, the flux scale is converted to the equivalent voltage magnitude with respect to the operating speed. It is shown that the pattern of $\hat{\lambda}_{pm\_\alpha}$ versus $\hat{\lambda}_{pm\_\beta}$ is similar to a circle where the radius is almost fixed at 0.59V. Besides at full load in (d), the reduced distortion on the flux pattern still achieves comparing to EMF pattern in (b). It is noted that the flux pattern in (d) changes from the circle to hexagon due to the flux saturation at full load. Nevertheless, better SNR's on $\hat{\lambda}_{pm\_\alpha}$ and $\hat{\lambda}_{pm\_\beta}$ still results even under a 1kHz high bandwidth current regulation. It is concluded that the dynamic response of sensorless drive can be maintained based on the flux-based estimation.

B. POSITION ESTIMATION ERROR

This part evaluates the position estimation performance using either the EMF voltage and flux linkage. Fig. 14 compares both EMF-based and flux-based position estimation using Fig. 14 (a) command voltages and (b) measured voltages.

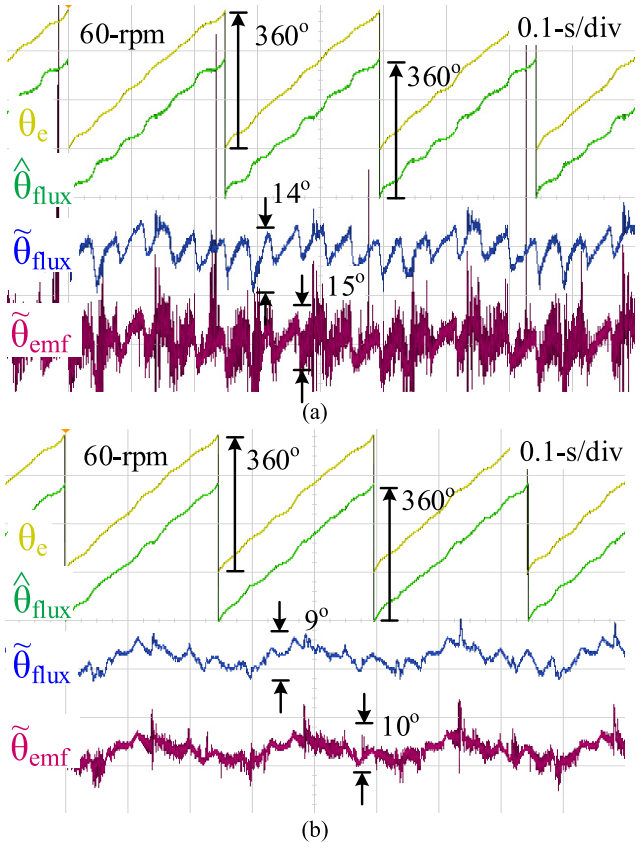

FIGURE 14. Comparison of EMF- and flux-based position estimation using (a) command voltages and (b) measured voltages (150% load, 60rpm and 2% speed).

In this test, the speed is controlled at 2% rate speed (60rpm) with 150% load. Time-domain signals of measured θ_e, estimated flux-based position $\hat{\theta}_{flux}$, EMF-based position error $\tilde{\theta}_{emf}$, and flux-based position error $\tilde{\theta}_{flux}$ are respectively shown. As seen in Fig. 14(a), visible deadtime reflected 6th-order harmonics on both $\tilde{\theta}_{emf}$ and $\tilde{\theta}_{flux}$ are observed by using command voltages for the estimation. Although dead-time harmonics occur on both estimation methods, the SNR of flux-based position error $\tilde{\theta}_{flux}$ is higher than that of EMF-based $\tilde{\theta}_{emf}$. In addition, Fig. 14(b) shows same waveforms while the measured voltages are used for EMF and flux estimation. By considering the inverter distortion for the estimation, 6th-order harmonics disappear in both $\tilde{\theta}_{emf}$ and $\tilde{\theta}_{flux}$. However, the SNR of $\tilde{\theta}_{flux}$ is still higher than $\tilde{\theta}_{emf}$. As a result, it is concluded that flux-based position estimation results in the better SNR. The deadtime harmonics can be further removed by using measured voltages for the estimation.

C. FLUX vs. EMF HARMONIC DISTORTION

This part analyzes secondary harmonics on the estimated EMF voltage and flux linkage. Fig. 15 compares the total harmonic distortion (THD) of $\hat{e}_\alpha$ and $\hat{\lambda}_{pm\_\alpha}$ with respect to different current regulator bandwidths and rotor operating speeds. The EMF or flux estimation using both command and measured voltages are all evaluated. Considering firstly EMF

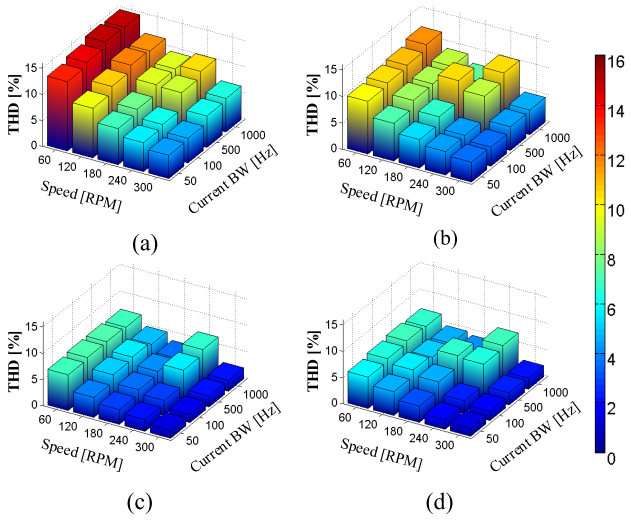

FIGURE 15. THD comparison of EMF estimation waveform using (a) command and (b) measured voltages, and flux estimation using (c) command and (d) measured voltages (full load).

harmonics using command voltages in (a), the THD increases as the increase of current bandwidth or the decrease of speed. More importantly, the THD of EMF significantly increases once the rotor speed is below 4% speed (120rpm), leading to the stability issue. By adding the phase voltage measurement in (b), the THD decreases for all operating conditions. However the physical limitation on EMF voltage still appears, as seen for THD at 2% speed. This low speed limitation can be improved by obtaining the flux linkage. Fig. 15(c) shows the estimated $\hat{\lambda}_{pm\_\alpha}$ using command voltages. It is seen that the THD's all decrease comparing the EMF THD in (a) and (b). The speed independent estimation performance is the primary advantage.

Finally for the flux estimation in (d) using measured voltages, the THD can further decrease at low speed and high bandwidth conditions. Fig. 16 analyzes the harmonic distribution of (a) $\alpha-$ axis estimated EMF $\hat{e}_\alpha$ and (b) $\alpha-$ axis estimated flux $\hat{\lambda}_{pm\_\alpha}$ at different speeds. The current bandwidth is set at 1kHz considering high dynamic applications. Command voltages are used to evaluate dead-time reflected harmonics. As seen from $\hat{e}_\alpha$ in Fig. 16(a), inverter deadtime causes 5th-order and 7th-order position harmonics, which greatly degrades the estimation accuracy. Their magnitudes increase as the speed decreases. The speed-dependent estimation performance on $\hat{e}_\alpha$ is the primary reason. By contrast, Fig. 16(b) shows the harmonic distribution of estimated flux $\hat{\lambda}_{pm\_\alpha}$. Comparing to $\hat{e}_\alpha$ in Fig. 16(a), 5th- and 7th-order harmonics all decrease by estimating the flux linkage. It is noted that 2nd-order harmonics also appear in both $\hat{e}_\alpha$ and $\hat{\lambda}_{pm\_\alpha}$. This harmonic might be induced by the machine asymmetric property since the harmonic magnitudes are the same on $\hat{e}_\alpha$ and $\hat{\lambda}_{pm\_\alpha}$.

D. CURRENT AND SPEED LOOP BANDWIDTH

This part experimentally analyzes the closed-loop current and speed controller bandwidth among encoder-based,

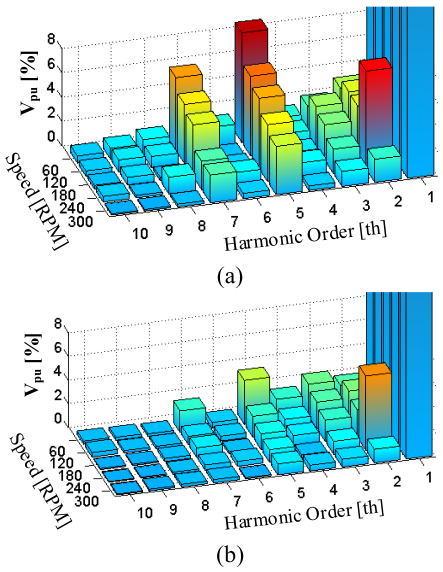

FIGURE 16. Harmonic distribution of (a) estimated EMF and (b) estimated flux at different speeds (full load and command voltage).

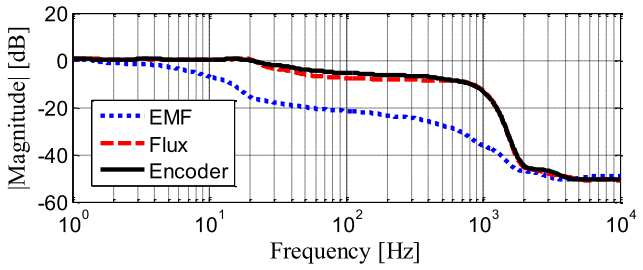

FIGURE 17. Frequency response of current controller at 10% rated speed among three different FOC drives.

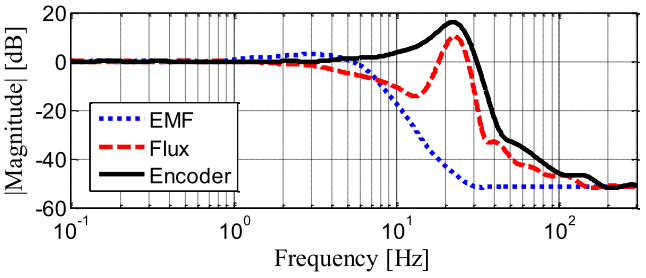

FIGURE 18. Frequency response of speed controller at 10% rated speed among three different FOC drives.

EMF-based and flux-based FOC drive. In these tests, the machine speed is controlled to maintain at 10% (300rpm) speed during the measurement process.

Fig. 17 demonstrates the frequency response of current controller among three different drives. The sweep AC current signal with 20% rated current is applied in d-axis from 1Hz∼10kHz. Considering the EMF-based drive, the current frequency response quickly decreases to −20dB around 50 Hz. The overall current controller bandwidth is around 100Hz which might not be suited for high dynamic applications. By contrast, the current bandwidth of flux-based drive is almost the same to the encoder-based drive where the maximum bandwidth is close to 1kHz though a slight

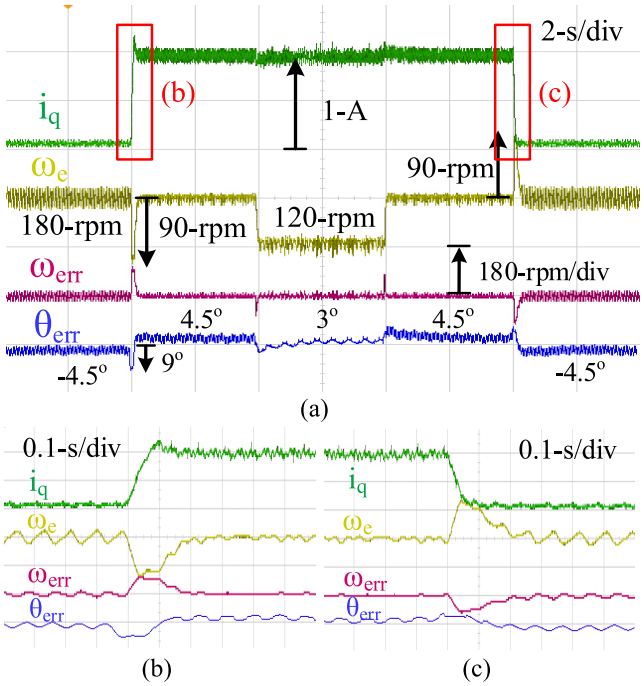

FIGURE 19. Speed closed-loop control under full step load using the proposed flux-based drive where (b) and (c) zoom the transient load response.

decay after 100Hz. Based on this comparison, it is concluded that the flux-based drive achieves the comparable current response to the standard servo drive under 10% rated speed.

Similarly, Fig. 18 shows the frequency response of speed controller at 10% speed among three FOC drives. Here, a small AC signal with ±60rpm is superimposed on the manipulated speed command 300rpm. This AC signal is swept from 0.1Hz to 300Hz. It is observed that the speed bandwidth of EMF-based drive is only 7Hz due to considerable estimation noises mentioned in Fig. 14. By contrast, the speed bandwidth of flux-based drive increases to 10Hz which is almost the same to the encoder-based drive. It is noted that similar to current frequency response, a similar magnitude decay is observed around 7∼20Hz on the flux-based drive. Nevertheless, the flux-based drive shows visible improvement on speed controller because of the better estimation SNR and lower secondary harmonics.

E. SPEED CONTROL UNDER THE STEP LOAD

This section evaluates the sensorless speed control performance under 100% step load. Fig. 19(a) shows the time-domain waveforms of i_q, ω_e, ω_{err} and θ_{err}.

In this test, the machine is controlled at 6% speed closed-loop. During the load operation, the speed is decelerated to 3% speed. Considering the step load transient, speed quickly recovers to the command speed within 0.2 sec as seen from zoom-in waveforms in Fig. 19(b) and (c). Besides, speed controller can also manipulate at 4% speed under full load. Thus, it is concluded that the proposed flux-based drive can achieve a high dynamic response while maintaining the stability at low speed.

V. CONCLUSION

This paper improves the SPM machine position sensorless drive through the modified flux estimation and phase voltage measurement. Comparing to EMF-based drive, key advantages of flux-based drive are summarized as follows:

- Flux-based drive has the better SNR on the position estimation. The better drive stability can be concluded especially at low speed.
- Inverter deadtime results in 5th- and 7th-order harmonics on the EMF-based position estimation. These two harmonics both reduced once the flux is used for the estimation.
- Flux-based sensorless drive achieves 1kHz current bandwidth at 10% speed. It is compatible to standard encoder-based drive.
- By using the proposed flux-based estimation, the SPM machine drive can operate under high dynamic step load and step speed at 6% speed.

REFERENCES

[1] S.-K. Kim, K.-G. Lee, and K.-B. Lee, "Singularity-free adaptive speed tracking control for uncertain permanent magnet synchronous motor," *IEEE Trans. Power Electron.*, vol. 31, no. 2, pp. 1692–1701, Feb. 2016.

[2] R. W. Hejny and R. D. Lorenz, "Evaluating the practical low-speed limits for back-EMF tracking-based sensorless speed control using drive stiffness as a key metric," *IEEE Trans. Ind. Appl.*, vol. 47, no. 3, pp. 1337–1343, May/Jun. 2011.

[3] Y. Park and S.-K. Sul, "A novel method utilizing trapezoidal voltage to compensate for inverter nonlinearity," *IEEE Trans. Power Electron.*, vol. 27, no. 12, pp. 4837–4846, Dec. 2012.

[4] N. Bedetti, S. Calligaro, and R. Petrella, "Self-commissioning of inverter dead-time compensation by multiple linear regression based on a physical model," *IEEE Trans. Ind. Appl.*, vol. 51, no. 5, pp. 3954–3964, Sep./Oct. 2015.

[5] M. H. Bierhoff, "A general PLL-type algorithm for speed sensorless control of electrical drives," *IEEE Trans. Ind. Electron.*, vol. 64, no. 12, pp. 9253–9260, Dec. 2017.

[6] L. Harnefors and H. P. Nee, "A general algorithm for speed and position estimation of AC motors," *IEEE Trans. Ind. Electron.*, vol. 47, no. 1, pp. 77–83, Feb. 2000.

[7] Y. Wang, Y. Xu, N. Niimura, B. D. Rudolph, and R. D. Lorenz, "Using volt-second sensing to directly improve torque accuracy and self-sensing at low speeds," *IEEE Trans. Ind. Appl.*, vol. 53, no. 5, pp. 4472–4482, Sep./Oct. 2017.

[8] A. Yoo and S.-K. Sul, "Design of flux observer robust to interior permanent-magnet synchronous motor flux variation," *IEEE Trans. Ind. Appl.*, vol. 45, no. 5, pp. 1670–1677, Sep./Oct. 2009.

[9] S. A. Davari, F. Wang, and R. M. Kennel, "Robust deadbeat control of an induction motor by stable MRAS speed and stator estimation," *IEEE Trans. Ind. Informat.*, vol. 14, no. 1, pp. 200–209, Jan. 2018.

[10] R. Morales-Caporal, E. Bonilla-Huerta, C. Hernandez, M. A. Arjona, and M. Pacas, "Transducerless acquisition of the rotor position for predictive torque controlled PM synchronous machines based on a DSP-FPGA digital system," *IEEE Trans. Ind. Informat.*, vol. 9, no. 2, pp. 799–807, May 2013.

[11] M.-H. Shin, D.-S. Hyun, S.-B. Cho, and S.-Y. Choe, "An improved stator flux estimation for speed sensorless stator flux orientation control of induction motors," *IEEE Trans. Power Electron.*, vol. 15, no. 2, pp. 312–318, Mar. 2000.

[12] J. Holtz and J. Quan, "Drift- and parameter-compensated flux estimator for persistent zero-stator-frequency operation of sensorless-controlled induction motors," *IEEE Trans. Ind. Appl.*, vol. 39, no. 4, pp. 1052–1060, Jul. 2003.

[13] R. Zhao, Z. Xin, P. C. Loh, and F. Blaabjerg, "A novel flux estimator based on multiple second-order generalized integrators and frequency-locked loop for induction motor drives," *IEEE Trans. Power Electron.*, vol. 32, no. 8, pp. 6286–6296, Aug. 2017.

[14] M. Moradian, J. Soltani, A. Najjar-Khodabakhsh, and G. R. A. Markadeh, "Adaptive torque and flux control of sensorless IPMSM drive in the stator flux field oriented reference frame," *IEEE Trans. Ind. Informat.*, vol. 15, no. 1, pp. 205–212, Jan. 2019.

[15] Z. Ma, J. Gao, and R. Kennel, "FPGA implementation of a hybrid sensorless control of SMPMSM in the whole speed range," *IEEE Trans. Ind. Informat.*, vol. 9, no. 3, pp. 1253–1261, Aug. 2013.

[16] F. Wang, Z. Chen, P. Stolze, J.-F. Stumper, J. Rodriguez, and R. Kennel, "Encoderless finite-state predictive torque control for induction machine with a compensated MRAS," *IEEE Trans. Ind. Informat.*, vol. 10, no. 2, pp. 1097–1106, May 2014.

[17] G. Scarcella, G. Scelba, M. Pulvirenti, and D. Robert Lorenz, "Fault-tolerant capability of deadbeat-direct torque and flux control for three-phase PMSM drives," *IEEE Trans. Ind. Appl.*, vol. 53, no. 6, pp. 5496–5508, Nov./Dec. 2017.

[18] M. Hinkkanen and J. Luomi, "Modified integrator for voltage model flux estimation of induction motors," *IEEE Trans. Ind. Electron.*, vol. 50, no. 4, pp. 818–820, Aug. 2003.

[19] J. Hu and B. Wu, "New integration algorithms for estimating motor flux over a wide speed range," *IEEE Trans. Power Electron.*, vol. 13, no. 5, pp. 969–977, Sep. 1998.

[20] G.-R. Chen and S.-C. Yang, "Phase voltage measurement for permanent magnet machine sensorless drive using controller capture modulator," *IEEE Trans. Ind. Electron.*, vol. 67, no. 1, pp. 49–58, Jan. 2020.

GUAN-REN CHEN (S'17) was born in Taiwan. He received the M.S. degree in opto-mechatronics engineering from National Central University, Taiwan, in 2014. He is currently pursuing the Ph.D. degree in mechanical engineering with National Taiwan University, Taipei, Taiwan. His research interests include control systems, motor drives, and intelligent vehicles.

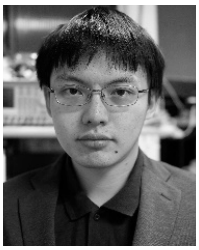

JYUN-YOU CHEN (S'19) was born in Taiwan in 1992. He received the B.S. degree in communication engineering from Feng Chia University, Taiwan, and the M.S. degree in mechanical engineering from National Central University, Taiwan, in 2015 and 2017, respectively. He is currently pursuing the Ph.D. degree in mechanical engineering with National Taiwan University, Taiwan. His research interests include motor drive and control.

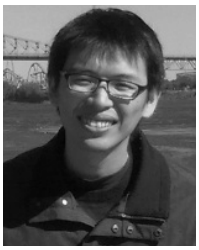

SHIH-CHIN YANG (S'10–M'12–SM'18) was born in Taiwan. He received the M.S. degree from National Taiwan University, Taiwan, and the Ph.D. degree from the University of Wisconsin–Madison, WI, USA, in 2007 and 2011, all in mechanical engineering. From 2011 to 2015, he was a Research Engineer with Texas Instruments Motor Lab., Dallas, TX, USA. He is currently an Associate Professor with National Taiwan University, Taiwan, with the responsibility on the development of motor drive and motor control technology. His research interests include motor drives, power electronics, and control systems. He was a recipient of the IEEE Industry Applications Society Industrial Drive Committee First Prize Paper Award, in 2011.